

Experiments in transverse gust mitigation using open-loop pitch maneuvers

Girguis Sedky* and Antonios Gementzopoulos[†] *University of Maryland, College Park, MD, 20742*

Francis D. Lagor[‡]
University at Buffalo, The State University of New York, Buffalo, NY, 14260

Anya R. Jones[§] *University of Maryland, College Park, MD, 20742*

This paper presents three open-loop pitch maneuvers with the objective of mitigating the lift transient during large-amplitude transverse wing-gust encounters. In the first maneuver, the wing's instantaneous geometric angle of attack opposes the effective angle of attack induced by the gust. In the second maneuver, the analytical lift result from an unsteady aerodynamic model based on the work of Wagner and Küssner sums to zero. In the third maneuver, the wing's pitch kinematics are obtained from closed-loop control simulations in an unsteady discrete vortex model (DVM). The open-loop pitch maneuvers were experimentally implemented for different gust ratios GR = $v_{g,\max}/U_{\infty}$, and force and flowfield measurements were collected. The lift coefficient as well as shed vortex circulation time histories of all the cases are compared to identify the flow physics responsible for lift attenuation. In addition, the flowfield's vorticity, vector fields, and streamlines of select cases are presented and analyzed. Finally, the DVM-simulated flow fields are compared to experimental flowfield measurements to assess its accuracy and viability for maneuver design.

I. Introduction

Unsteady flow conditions present a challenge to stable flight [1–3], and gust rejection remains a concern for flight control [4]. Large-amplitude transverse gust encounters represent a canonical unsteady flow condition that has been the focus of many studies dating back to the 1930s. In 1932, Küssner [5] studied vertical gust encounters theoretically using potential flow modeling, and experimentally by measuring airplane wing deflection in stormy weather. According to Küssner, vertical or transverse gusts are particularly important because they lead to the highest wing stresses when compared to stresses caused by similar strength gusts in other directions. Küssner simulated the effect of a vertical gust on a wing by attributing to it a change in the angle of attack, a modeling problem solved earlier by Wagner [6]. The sharp-edged gust model developed by Küssner assumes a linear flow with a planar wake, attached flow, and the absence of viscosity. Nevertheless, it has been shown to predict loads outside of these assumptions [7].

During flapping flight, Ellington et al. [8] showed the significant influence that coherent structures such as the leading-edge vortex (LEV) can have on lift. Comprehensive gust-encounter studies that also reveal coherent structures are now possible using time-resolved particle image velocimetry (PIV) or computational fluid dynamics. Perrotta and Jones [9] used time-resolved PIV and force measurements to study transverse sine-squared wing-gust encounters at various angles of attack and gust strengths, where gust ratio is defined as the ratio of the maximum gust velocity to the freestream

$$GR = \frac{v_{g,\text{max}}}{U_{\infty}}.$$
 (1)

This work revealed important correlations between the force histories and coherent flow structures. The lift peak coincided with the formation of a strong LEV. A subsequent lift deficit coincided with the shedding of the LEV and the

^{*}Graduate Research Assistant, Department of Aerospace Engineering.

[†]Graduate Research Assistant, Department of Aerospace Engineering.

[‡]Assistant Professor, Department of Mechanical and Aerospace Engineering, AIAA Senior Member.

[§]Professor, Department of Aerospace Engineering, AIAA Associate Fellow.

formation of a trailing-edge vortex (TEV). The lift deficit was followed by a secondary lift peak that coincided with the formation of a second LEV. These observations suggest how specific coherent flow structures influence lift during transverse gust encounters.

Corkery et al. [10] developed a top-hat transverse gust encounter test apparatus and collected flow visualization, PIV, and force measurements for a wing-gust encounter for a gust ratio of 1.0. Similar to Perrotta and Jones, they observed the formation of a strong LEV during the encounter. In addition, they observed the deformation of the shear layers on the boundaries of the gust. These observations reveal violations of the attached-flow and a non-deforming gust assumptions made in gust-encounter classical theory. Despite differences in flow topology between theory and experiment, the authors found that lift force coefficients matched well during entry into the gust, but deviated upon exit. Andreu-Angulo et al. [11] expanded these studies by comparing gust encounters with a sine-squared profile and a top-hat profile. Their tests spanned gust ratios 0.5 to 1.5 as well as angles of attack 0° to 20°. They attributed a large discrepancy between the forces measured during same-strength but different-profile gusts to the significant difference in gust shear layer distribution between the two gust profiles, as well as the higher level of circulation shed during the top-hat gust. These recent studies have shed light on some of the main flow mechanisms that govern the aerodynamics of transverse gust encounters, which are possible targets for control design.

Recent studies have introduced pitching for the purposes of gust mitigation. In prior work, [12], the authors represented an unsteady sine-squared gust encounter for various gust ratios using a discrete vortex model (DVM). The authors proposed proportional feedback control to regulate lift during the encounter. To tune the gain of the feedback controller, the lift response to pitching was modeled using Theodorsen's unsteady aerodynamic model, and the lift response to the gust was modeled as an additive disturbance to the lift signal. The only known parameter for the gust was the reduced frequency range. A closed-loop controller based on proportional feedback of the measured lift was designed to provide a pitch acceleration input. The control gain was tuned using Theodorsen's (linear) aerodynamic model. The controller was tested in the (nonlinear) discrete vortex model, and performed well despite of the various assumptions implicit in the use of Theodorsen's model for tuning, such as attached flow and a planar wake. The authors decomposed the forces into a circulatory contribution caused by the evolution of vorticity in the wing's wake, an added-mass contribution caused by the wing's unsteady pitching motion, and a non-circulatory contribution from the gust itself. A reduction in the circulatory contribution to the lift force correlated with a reduction in circulation shed by the leading and trailing edges of the wing. During control maneuvers to mitigate the gust, the DVM simulations suggested that the non-circulatory gust contribution was canceled by the added-mass contribution due to the pitching of the wing. The present work provides experimental evidence to support these prior simulation-based findings in one of the maneuvers studied. Andreu-Angulo and Babinsky [13] demonstrated gust mitigation under the effect of an open-loop maneuver informed by unsteady aerodynamic theories of Küssner and Wagner. The coefficient of lift C_I of a gust encounter was calculated using Küssner's gust model, and a pitching profile was chosen such that Wagner's lift response canceled Küssner's gust response. Although this method required knowledge of the gust a priori, it was effective at gust mitigation, thereby providing further evidence for the usefulness of classical aerodynamic theory in control design for gust mitigation.

This paper contributes to the study of lift regulation in gust encounters by experimentally implementing and comparing three different open-loop (i.e., prescribed prior to the run) control maneuvers for gust mitigation. The first maneuver is designed such that the pitching angle of attack opposes the effective angle of attack induced by a non-deforming model of the gust. The effective angle of attack induced by the gust is obtained using quasi-steady thin airfoil theory and takes into account the non-uniform velocity distribution along the wing's chord. The second maneuver is designed, similar to [13], such that the analytical lift result from Wagner and Küssner unsteady aerodynamic models cancel out. The third maneuver is obtained from closed-loop control simulations in an unsteady discrete vortex model. The contributions of this work are (1) experimental demonstration of three open-loop control maneuvers for gust attenuation, based on: i) effective angle of attack, ii) a zero lift in a Wagner-Küssner model, and iii) a simulation of closed-loop proportional feedback control in a discrete vortex model, (2) an analysis of the physical mechanisms of lift mitigation and unmodeled effects in these three methods, and (3) an analysis of the use of discrete vortex models (DVMs) for maneuver design based on a comparison of DVM simulated flow fields with resulting experimental PIV measurements. Although the three maneuvers are open-loop in nature, these contributions are important because they provide further insight into useful mechanisms for force regulation in a gust encounter.

II. Aerodynamic modeling for maneuver design

This section introduces the aerodynamic models and control design techniques used to design the three open-loop maneuvers examined in this work: a maneuver based on effective angle of attack, a Wagner/Küssner maneuver, and a maneuver based on a closed-loop DVM simulation.

A. Maneuver based on effective angle of attack

The vertical upwash imposed on the wing by a transverse gust induces an effective angle of attack on the wing. Since the velocity of the gust may vary across the wing's chord, so does the local angle of attack. Figure 1 illustrates local variations in effective angle of attack induced by an upwash. An effective angle of attack expression that integrates the local angle of attack along the chord was derived in Sedky et al. [14] based on quasi-steady thin airfoil theory.

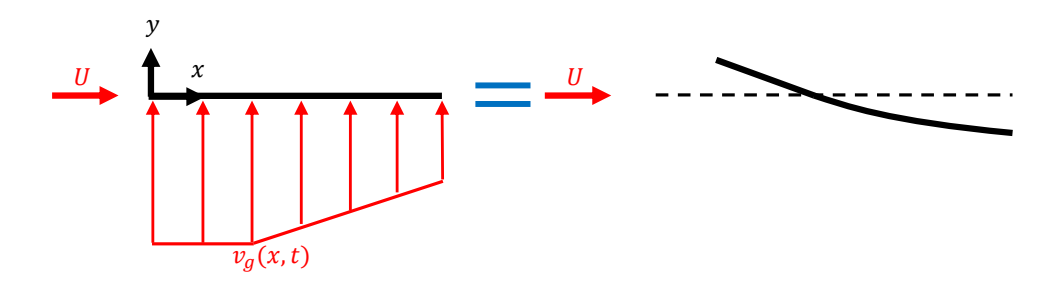


Fig. 1 Effective angle of attack induced by the gust

The effective angle of attack $\alpha_{\rm eff}$ due to a gust profile is

$$\alpha_{\text{eff}}(t) = -\frac{1}{\pi} \int_0^{\pi} \frac{v_g(\theta, t)}{U_{\infty}} (\cos \theta - 1) d\theta, \tag{2}$$

where v_g is the local transverse velocity at a point along the wing's chord, U_{∞} is the freestream velocity, and θ is the angular chord position. The angular chord position θ is related to the x location along the chord via the transformation

$$x = \frac{c}{2}(1 - \cos\theta),\tag{3}$$

where c is the chord length of the wing.

The open-loop pitch maneuver based on canceling the effective angle of attack relies on pitching the wing according to a priori knowledge of the gust to produce an angle of attack α such that $\alpha = -\alpha_{\rm eff}$. Of the maneuvers in this work, the effective angle of attack maneuver is the simplest to calculate. However, it fails to account for the added-mass force associated with acceleration of the fluid surrounding the body during unsteady motions. The maneuver does not account for the wake generated by the wing, which influences the circulatory lift. It assumes fully attached flow, and thus fails to model the formation of leading-edge vortices which have been observed in this work and many prior experimental studies [7, 9, 10]. Nevertheless, the effective angle of attack maneuver is considered in this work to assess the impact of unmodeled flow physics on gust mitigation.

B. Maneuver based on the Wagner and Küssner unsteady aerodynamic models

Linear superposition of Wagner's and Küssner's unsteady aerodynamic models produces an unsteady analytical model for a pitching wing in a transverse gust. A formulation similar to the one in this work is presented in [13].

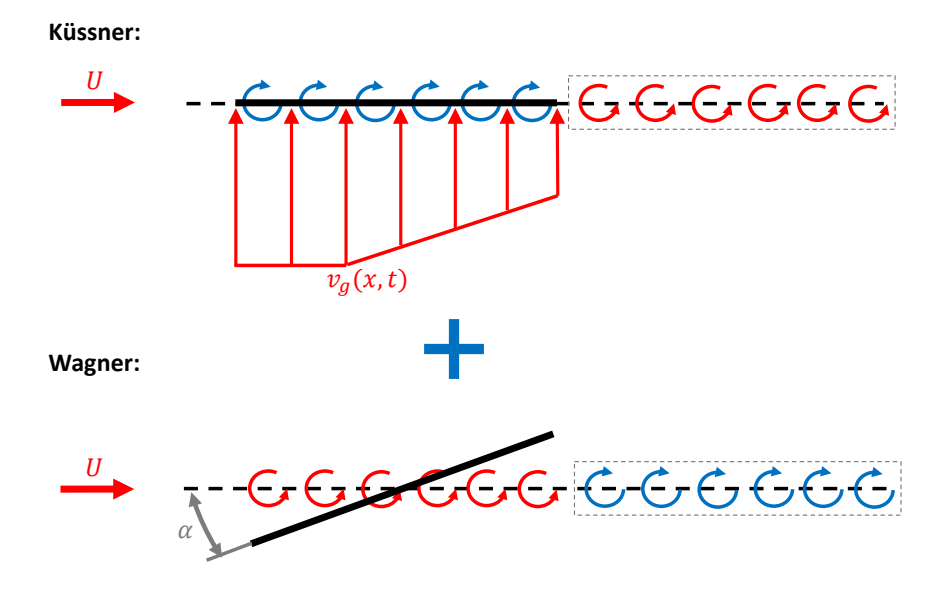


Fig. 2 The superposition of the Wagner and Küssner aerodynamic models

Wagner's indicial aerodynamic response provides the lift response of a wing due to a step response in angle of attack. Due to the linearity of the model, we can obtain the response to any continuous angle-of-attack profile through the convolution with Wagner's indicial function ϕ in the Duhamel integral. The non-dimensional lift response to an arbitrary angle-of-attack profile is [15]

$$C_L = 2\pi \int_0^s \frac{\mathrm{d}\alpha}{\mathrm{d}\sigma} \phi(s - \sigma) \mathrm{d}\sigma, \tag{4}$$

where s is the distance traveled by the wing in semi-chords, σ is a dummy integration variable. Wagner's function based on R.T. Jones' [16] approximation is

$$\phi(s) = 1 - 0.165e^{-0.0455s} - 0.335e^{-0.3s}.$$
 (5)

Wagner's aerodynamic model captures the wake shed from the wing during the unsteady maneuver, which is not captured by the induced angle of attack method.

Küssner's unsteady aerodynamic model captures the lift response of a wing to a semi-infinite uniform gust. Similar to Wagner's model, we can also obtain the lift response through the convolution with an indicial function. Küssner's lift response to an arbitrary gust is

$$C_L = \frac{2\pi}{U_{\infty}} \int_0^s \frac{\mathrm{d}v_g}{\mathrm{d}\sigma} \psi(s - \sigma) \mathrm{d}\sigma, \tag{6}$$

where v_g is the transverse velocity the wing experiences at its leading edge and ψ is Küssner's function. Küssner's function based on Sears and Sparks approximation is [17]

$$\psi = 1 - 0.5e^{-0.13s} - 0.5e^{-s}. (7)$$

The aforementioned models do not capture the added-mass effect from pitching, and thus an additional term for the added-mass force of a wing pitching about the midchord must be added. Under small-angle assumptions, the added-mass lift force experienced by a wing due to pitching about the midchord is

$$C_L = \frac{\pi c}{2U_{\infty}} \dot{\alpha}. \tag{8}$$

Thus, the combined model for a pitching wing encountering a gust is

$$C_L = 2\pi \int_0^s \frac{\mathrm{d}\alpha}{\mathrm{d}\sigma} \phi(s - \sigma) \mathrm{d}\sigma + \frac{2\pi}{U_\infty} \int_0^s \frac{\mathrm{d}v_g}{\mathrm{d}\sigma} \psi(s - \sigma) \mathrm{d}\sigma + \frac{\pi c}{2U_\infty} \dot{\alpha}. \tag{9}$$

Model 9 captures the unsteady effects of the wing's wake, the influence of the gust, and the added-mass force due to pitching about the midchord. However, this model assumes fully attached flow and a small angle of attack. Maneuvering in strong gusts violates these assumptions due to fully separated flows and large angular displacements. However, model 9 serves as an important point of comparison since it represents classical, linear aerodynamic modeling.

C. Proportional feedback control in a discrete-vortex simulation

Consider an open-loop maneuver computed from a closed-loop control simulation within an unsteady discrete vortex model (DVM). In this DVM, a flat plate is modeled by an infinitely thin sheet composed of a series of control points and bound vortices. Leading- and trailing-edge shedding is enforced by the Kutta condition at both edges of the wing. The gust is modeled as a velocity field, and the transverse velocity contribution of the gust is imposed on the wing's control points, bound vortices, and shed vortices according to their positions within the gust. The prior work of the authors [12] provides additional information on the construction of the DVM.

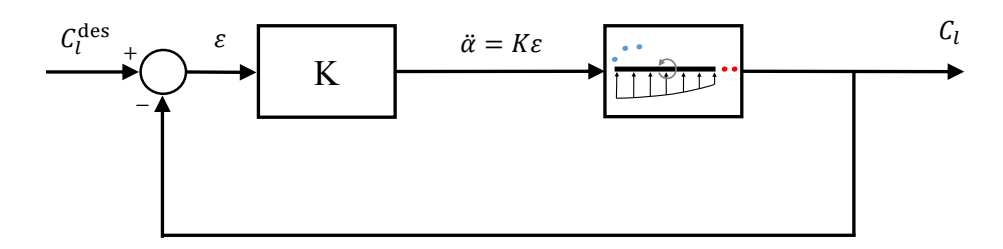


Fig. 3 Closed-loop control structure for DVM simulation

Figure 3 shows the output-feedback control framework used to regulate the lift of a wing about a desired value, C_L^{des} . In this proportional output-feedback control framework, the pitch acceleration control $\ddot{\alpha} = K\varepsilon$ is proportional to the current value of the error, $\varepsilon = C_L^{\text{des}} - C_L$. The calculated control input pitches the wing in the unsteady DVM, resulting in a corresponding lift response. The measured lift C_L feeds back back, closing the control loop. The controller gain is chosen to provide good disturbance rejection for an expected range of gust frequencies. The prior work of the authors [12] contains additional information on gain selection for the controller which is based on a linear Theodorsen model. Using this gain value, the closed-loop control DVM simulation creates a control profile by responding to the lift force calculated in the DVM model. Although this maneuver is closed-loop in the DVM simulation (i.e. it responds to real-time changes in the flow model), the maneuver is executed open-loop in experiment in this paper.

D. Summary of open-loop maneuvers

Three open-loop maneuvers are constructed and experimentally implemented in this work. The first maneuver relies on creating an angle of attack trajectory $\alpha(t)$ that opposes the effective angle of attack induced by the gust,

$$\alpha_{\text{eff}}(t) = -\frac{1}{\pi} \int_0^{\pi} \frac{v_g(\theta, t)}{U_{\infty}} (\cos \theta - 1) d\theta, \tag{10}$$

such that $\alpha(t) + \alpha_{\text{eff}}(t) = 0$. The second maneuver relies on pitching the wing in a Wagner-Küssner aerodynamic model to achieve

$$C_L = 2\pi \int_0^s \frac{\mathrm{d}\alpha}{\mathrm{d}\sigma} \phi(s - \sigma) \mathrm{d}\sigma + \frac{2\pi}{U_\infty} \int_0^s \frac{\mathrm{d}v_g}{\mathrm{d}\sigma} \psi(s - \sigma) \mathrm{d}\sigma + \frac{\pi c}{2U_\infty} \dot{\alpha} = 0.$$
 (11)

To obtain the pitch profile $\alpha(t)$ from the zero lift constraint 11, $\dot{\alpha}$ is discretized using the forward-Euler method such that

$$\dot{\alpha} = \frac{\alpha(t_{k+1}) - \alpha(t_k)}{\Delta t},\tag{12}$$

and 11 is solved for $\alpha(t_{k+1})$ where $t_k = k\Delta t$ for k = 0, ..., N. The third maneuver is extracted from an unsteady DVM simulation of the wing-gust encounter with the proportional control law

$$\ddot{\alpha} = K \left(C_L^{\text{des}} - C_L \right), \tag{13}$$

that is designed to mitigate deviations in lift from the desired value. For brevity, each maneuver name is abbreviated in this work. The effective angle-of-attack derived maneuver, the Wagner-Küssner derived maneuver, and the closed-loop discrete-vortex-model derived maneuver are referred to as 'Eff.-D', 'WK-D', and 'DVM-D', respectively. Figure 4 shows the angle-of-attack and pitch time histories of the wing for each maneuver at GR = 0.50. The gray region indicates the time in which the wing is at least partially within in the gust.

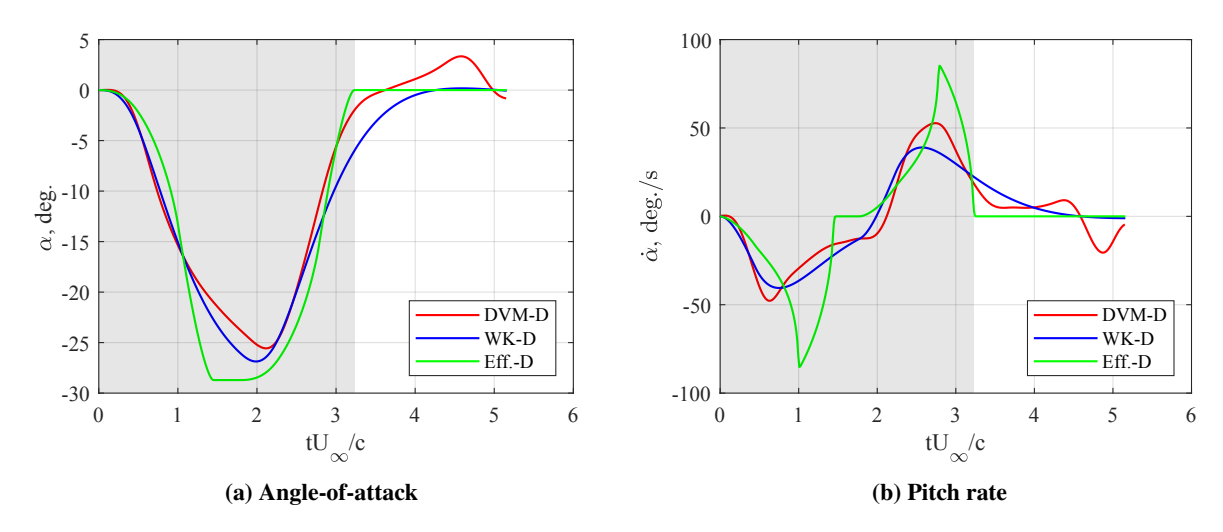


Fig. 4 The angle-of-attack and pitch rate for three prescribed maneuvers at GR = 0.50

The three maneuvers differ based on the modeling approach used in the construction of each. The Eff.-D maneuver relies on an attached flow assumption and does not model the wake effects or added mass. The WK-D maneuver retains the attached flow assumption but incorporates wake effects and added mass. The DVM-D model contains both wake and added-mass effects. Moreover, the DVM-D model relaxes the assumption of attached flow by representing shed vortices from the leading and trailing edges using discrete vortices.

III. Experimental methodology

This section introduces the experimental setup and describes the approach and methodology for force and flowfield data acquisition.

A. Experimental setup and test matrix

Wing-gust encounter experiments were conducted in a $7 \times 1.5 \times 1$ m free-surface water tow tank at the University of Maryland where a computer-controlled motor system towed the wing through the water tank. Figure 5 shows an overview of the experimental set-up and the half-wing test article used in the experiments. The half-wing model used in this work was a flat-plate with a chord length of c = 0.0762 m, an effective aspect ratio of R = 4, and a thickness-to-chord ratio of 0.0417. The wing was made of glass to minimize laser sheet shadows in flowfield images. Experiments were conducted at a Reynolds number Re = 10,000.

A gust generator provided a transverse gust flowfield at the center of the water tow tank. The transverse gust has a trapezoidal profile, and the gust-width-to-chord ratio is w/c = 2.23. A variable-speed 1.85 HP Hayward centrifugal pump drove the recirculating gust system. More details regarding the design of the gust generator can be found in [18]. The wing mounted onto an ATI Mini-40 force sensor. A divider or splitter plate isolated the half-wing from any flow disturbance caused by the pitching mechanism or force balance. Pitching actuation was accomplished by fixing the vertical height of the leading control rod and varying the vertical height of the trailing control rod, resulting in a pitch axis located at the wing's midchord.

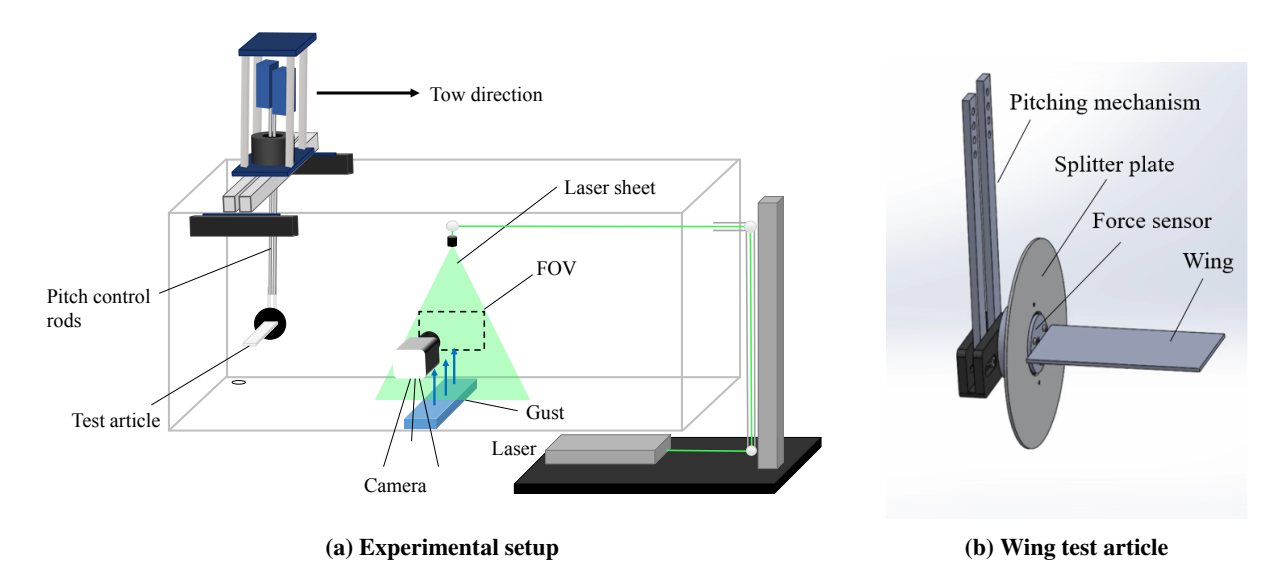


Fig. 5 An overview of the experimental set-up and the wing test article used

Table 1 shows the experimental cases considered in this work. The total number of cases presented was 12, and each case was repeated five times and ensemble averaged. The wing was towed in the water tank with a smoothed trapezoidal velocity profile. The wing was accelerated for 4.5 chords, towed at a constant velocity for 50 chords, and then decelerated for 2.25 chord to a full stop. The start of the gust region at the height of the test article was approximately 35.5 chords away from the wing's start position.

Table 1 Test matrix

Maneuver	Gust ratio
No pitch	0.25, 0.50, 0.61
$\alpha_{\rm eff}$ derived (EffD)	0.25, 0.50, 0.61
Wagner and Küssner derived (WK-D)	0.25, 0.50, 0.61
Closed-loop DVM derived (DVM-D)	0.25, 0.50, 0.61

B. PIV and force measurements

Forces and moments in all three axis were sampled at 1 kHz and recorded using a six degree-of-freedom ATI Mini-40 force sensor. The force sensor was mounted at the midchord of the wing to measure loads and moments at the midchord. Since the force sensor rotates with the wing during the pitching motion, sweeps were conducted in the range of expected pitch angles to tare the sensor at all expected orientations. The tare force and moment measurements account for sensor bias, the weight of the test article, and the buoyancy force. The raw measurements were filtered using a zero-phase digital Butterworth filter with a cutoff frequency of 5 Hz. The coefficient of lift C_L

$$C_L = \frac{L}{1/2\rho U_\infty^2 S},\tag{14}$$

was obtained by dividing the lift force by the dynamic pressure $1/2\rho U_{\infty}^2$ and the wing's planform area S.

Planar PIV measurements of the flow were collected during the wing-gust encounters. The PIV setup consisted of a Quantel Evergreen Nd:YAG 532 nm laser and a high-speed Phantom v641 camera with a 2560×1600 resolution. The laser sheet illuminated neutrally buoyant class IV soda lime spheres of 37 μ m diameter. The time separation between images within a pair Δt was chosen such that the maximum particle displacement of particles across an image pair is 4-5 pixels. The raw images acquired were processed using multi-pass cross-correlation. A 64 \times 64 px square interrogation window was used for the first four passes and a 24×24 px adaptive interrogation window was used for the following

four passes. Interrogation regions were overlapped by 50%. Post-processing was performed using a median universal outlier filter with a 5×5 filter region for the gust encounter cases. All force and flowfield measurements were ensemble averaged for each case.

IV. Results and discussion

A. Force measurements

A wing encountering a gust and undergoing an unsteady pitching maneuvers experiences lift from multiple sources. One of the main contributions to lift is the added-mass force. The added-mass coefficient of lift $C_L^{\rm am}$ of a wing pitching about its midchord based on potential flow theory can be expressed as [14]

$$C_L^{\rm am} = \frac{\pi c}{2U_\infty} \dot{\alpha} \cos^2 \alpha,\tag{15}$$

where the cosine term accounts for the large angle of attack displacements that may be undertaken by the wing. The total lift coefficient, C_L , can be decomposed into an added-mass force contribution, C_L^{am} , and a contribution based on the remainder of the flow, C_L^{rem} , such that

$$C_L = C_L^{\text{am}} + C_L^{\text{rem}}. (16)$$

The remainder of the lift contains the circulatory contribution due to the vortex shedding behavior of the wing as well as a non-circulatory contribution due to the flowfield imposed by the gust. The latter contribution was not decomposed further because the flowfield imposed by the gust varies during the encounter.

Figures 6a to 6c present the histories of the total coefficient of lift C_L , added-mass contribution $C_L^{\rm am}$, and the remainder of the lift coefficient $C_L^{\rm rem}$, respectively. All cases are normalized by the gust ratio GR. Each maneuver is shown with a different color and each GR is shown with a different line style. Each line is the ensemble average of five runs. The gray region in the plots highlights the portion where the wing is at least partially within the gust. Even though the results across gust ratio have different magnitudes, they collapse across gust ratios when they are normalized by the gust ratio value.

Figure 6a shows the total lift trends. For the no-pitch cases, the C_L trends climb up to $C_L=4$ GR before dropping down to 0 as the wing fully exits the gust. The Eff.-D maneuvers perform the worst at mitigating the influence of the gust at all gust ratios. The DVM-D and the WK-D maneuvers perform similarly until the wing begins to exit the gust. Thereafter, the WK-D maneuvers regulate lift better, indicating that the DVM may not accurately capture the flowfield during the wing's exit from the gust. Note that Fig. 4 shows the DVM-D maneuver performs significantly more actuation of the wing after $tU_{\infty}/c=4$ than the other maneuvers due to the continued presence of shed vorticity near the wing. The other maneuvers rely on non-deforming gust models for which the lift deviations taper off after exiting the gust. Figure 6b shows the added-mass force contribution, C_L^{am} , due to pitching of the wing. All three open-loop maneuver design methods result in pitch-down then pitch-up motion as seen in Fig 4. As the wing enters the gust the pitch down behavior acts to reduce the relative flow velocity normal to the chord. The motion leads to a negative added-mass force peak according to Eq. 15. As the wing exits the gust, it pitches back up, leading to a positive added-mass force peak. Figure 6c shows the remainder of the lift coefficient, $C_L^{\rm rem}$, time histories, which are a function of the circulatory forces due to the vortex shedding behavior of the wing as well as the non-circulatory forces due to the gust's flowfield. The $C_L^{\rm rem}$ time histories show trends opposite to the $C_L^{\rm am}$ trends. As the wing enters the gust, $C_L^{\rm rem}$ increases to a peak value. Following this increase, $C_L^{\rm rem}$ decreases back to a relatively constant value around $tU_{\infty}/c=1.60$. As the wing exits the gust, $C_L^{\rm rem}$ achieves a negative peak and then returns to zero after the wing fully exits the gust.

The force decomposition presented in Fig. 6a highlights how the pitch maneuvers mitigate lift. The pitching maneuvers reduce the circulatory contribution due to the vortex shedding which is captured by $C_L^{\rm rem}$. The remaining $C_L^{\rm rem}$ contribution is counter-balanced by the added-mass force contribution $C_L^{\rm am}$ due to pitching of the wing. Figure 6b shows significant differences in $C_L^{\rm am}$ across different maneuver-design methods and gust ratios, which results from differences in $\dot{\alpha}$ across maneuvers, as shown in Fig. 4b. In contrast to the $C_L^{\rm am}$ histories across different maneuvers, the remainder lift coefficient, $C_L^{\rm rem}$, trends are similar across different maneuvers. This similarly indicates that differences in lift regulation across maneuvers are primarily due to differences in the added-mass force. In addition, the groupings and relative positions of the $C_L^{\rm rem}$ curves across different maneuvers matches the grouping and positions of the relative α trajectories shown in Fig. 4a, indicating that the lift remainder $C_L^{\rm rem}$, which contains a large circulatory component, may be primarily influenced by the angle of attack of the wing.

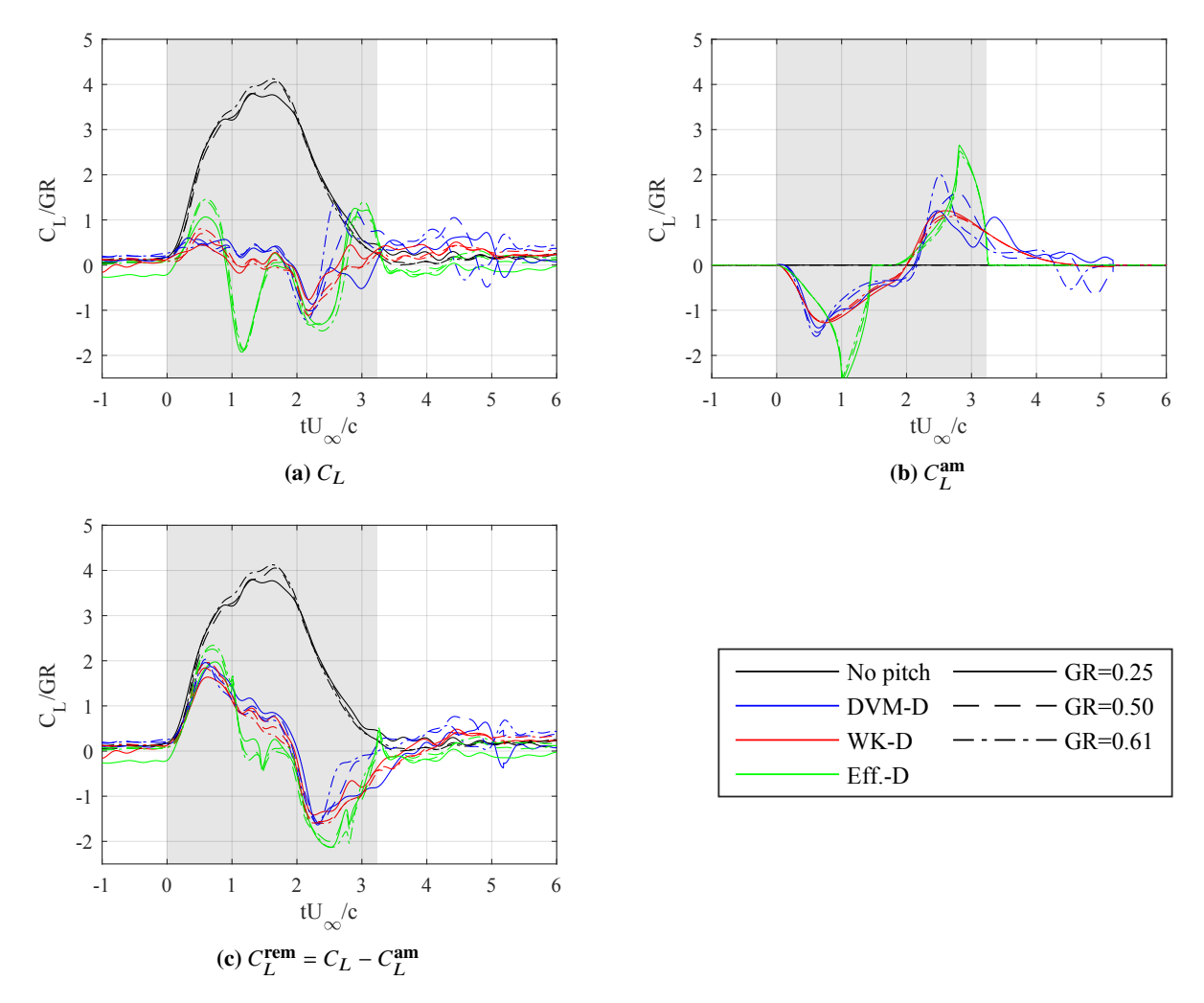


Fig. 6 The total coefficient of lift C_L , the added-mass contribution C_L^{am} , and the remainder of the coefficient of lift C_L^{rem} for all cases normalized by GR

B. Flowfield measurements

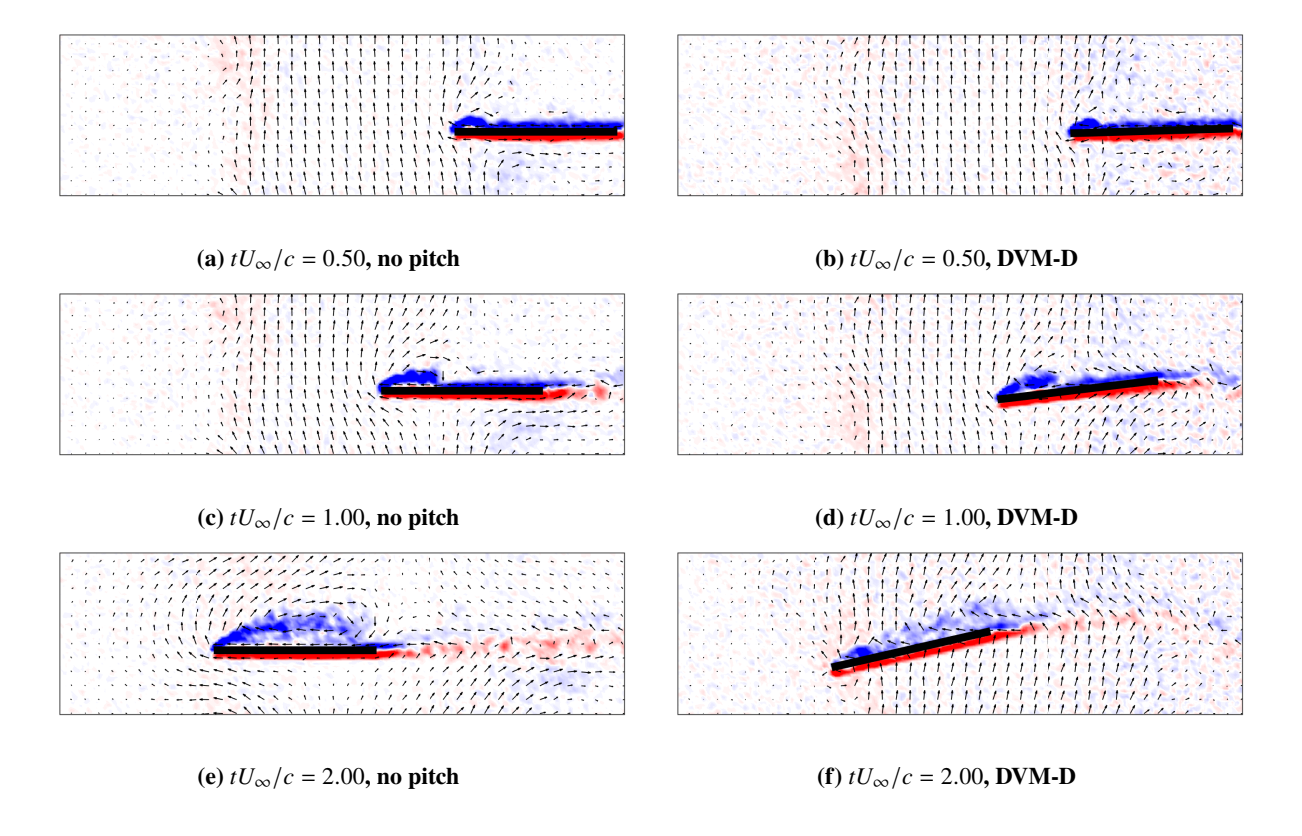
Figures 7 and 8 show the flowfields of the gust encounters without pitching (first column) and under DVM-D pitching (second column) for gust ratios GR = 0.25 and GR = 0.50, respectively. Each row corresponds to a specific convective time instant. The wing first encounters the gust at $tU_{\infty}/c = 0$ for all cases. The flowfields of the other cases are qualitatively similar, and are thus not presented. The flowfields presented consist of velocity vectors and non-dimensional vorticity fields, $\omega c/U_{\infty}$. For the clarity of the figures, only every fifth vector in the vector field is shown.

In the left column of Fig. 7, as the non-maneuvering wing enters the gust, the upwash creates a strong leading-edge shear layer and a subsequent LEV at $tU_{\infty}/c = 1.00$. The shear layer continues to feed vorticity to the LEV, and the vortex grows until it separates. Due to the low gust ratio, the LEV does not fully separate from the wing's suction side and stretches across the surface, as shown at $tU_{\infty}/c = 2.00$. As the wing reaches the latter half of the gust, the leading-edge shear layer feeding the LEV is disrupted. The LEV is shed at approximately $tU_{\infty}/c = 2.75$. The separated vortex loses form as it convects away. Throughout the gust encounter, the trailing-edge wake of the non-maneuvering wing experiences an upwash from the gust, causing it to bend slightly upwards. Throughout the encounter, the transverse gust flow stagnates on the pressure side of the wing. The passage of the wing through the gust disturbs the flow, and the disturbance to the flow persists after the wing completely exits the gust as shown at $tU_{\infty}/c = 6.00$.

In the right column of Fig. 7, a maneuvering wing executes a DVM-D pitching motion. As the wing enters the gust, it starts to pitch down, and as in the encounter without pitching, an LEV develops. The LEV of the maneuvering

wing detaches sooner than the LEV on the non-maneuvering wing. As the wing exits the gust, it pitches up and an opposite-signed LEV forms on the pressure side of the wing. To distinguish between the primary LEV that forms as the wing enters the gust and the second LEV that forms as the wing exits the gust under pitch control, the former will be referred to as the suction-side LEV and the latter will be referred to as the pressure-side LEV. In contrast to the case without pitching, the flow on the pressure side does not exhibit the same stagnation flow. Instead, the velocity vectors maintain a large vertical component. This flow behavior is physical and consistent with the no-penetration boundary condition in the lab frame. In this frame, the wing is translating as well as pitching. Thus, the wing's surface has a non-zero vertical velocity component that the fluid parcels on the wing's surface must match to satisfy the no-penetration and no-slip boundary conditions. The pitching motion seems to reduce the disturbance to the gust's flowfield as shown in each of the plots in the second column of Fig. 7. Through minimization of the gust's deformation, the wing reduces the momentum transfer between the two systems, thus reducing the lift transient experienced.

In the left column of Fig. 8, the non-maneuvering gust encounter at GR = 0.50 experiences the same general trends seen for GR = 0.25. The gust is stronger, which leads to a strong suction-side LEV. This LEV induces the formation of secondary vorticity under it, as shown at $tU_{\infty}/c = 1.00$. The suction-side LEV grows in size, convects upwards, and separates. The trailing-edge wake deflects upwards significantly more compared to the GR = 0.25 case. The wing's disturbance to the gust is severe and leads to the formation of two large vortices on either sides of the gust. These vortices are also seen when the gust generator is first turned on, which indicates that the passage of the wing though the gust is similar to an abrupt blockage and subsequent restart of the gust flow. This action leads to a large transfer of momentum between the gust and the passing wing, increasing the lift overshoot experienced by the wing. In the right column of Fig. 8, the pitching wing's suction-side LEV detaches faster than the case without pitching. As the wing exits the gust, a pressure-side LEV as well as a trailing-edge vortex form. As with pitching at GR = 0.25, the flowfields in the right column of Fig. 8 show that the pitching appears to minimize the disturbance of the gust flowfield.



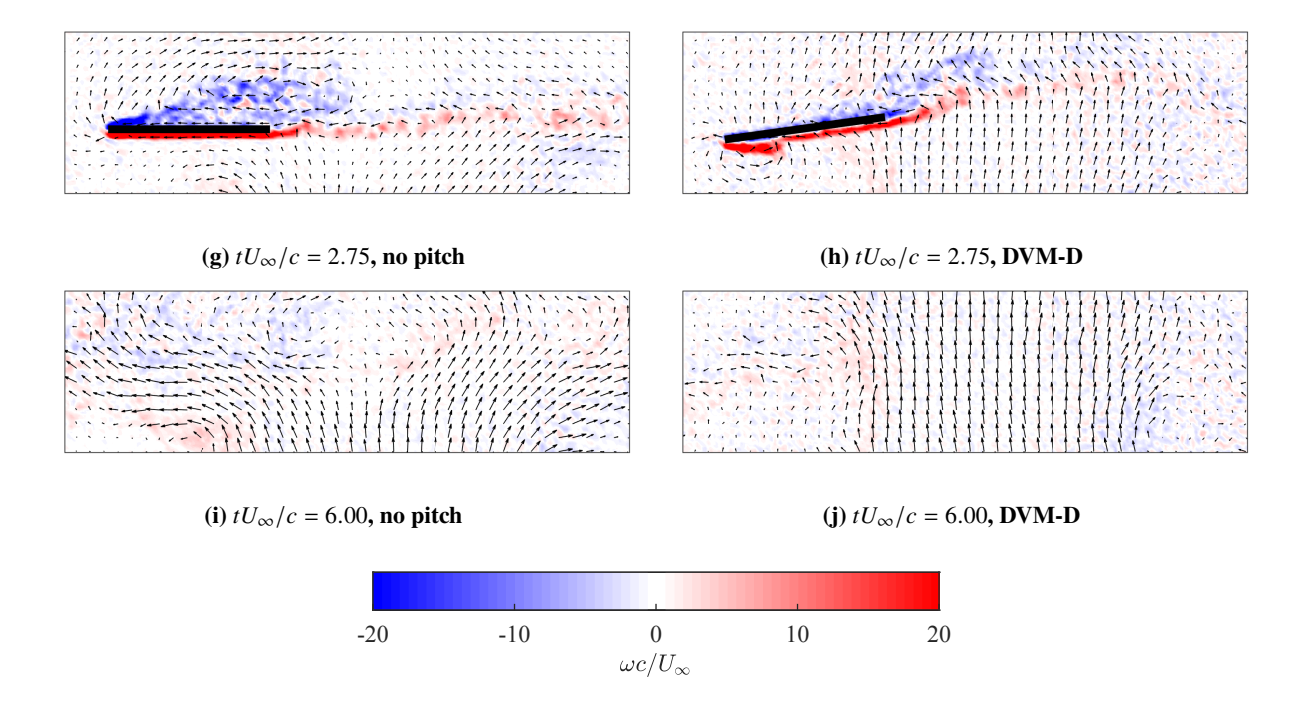
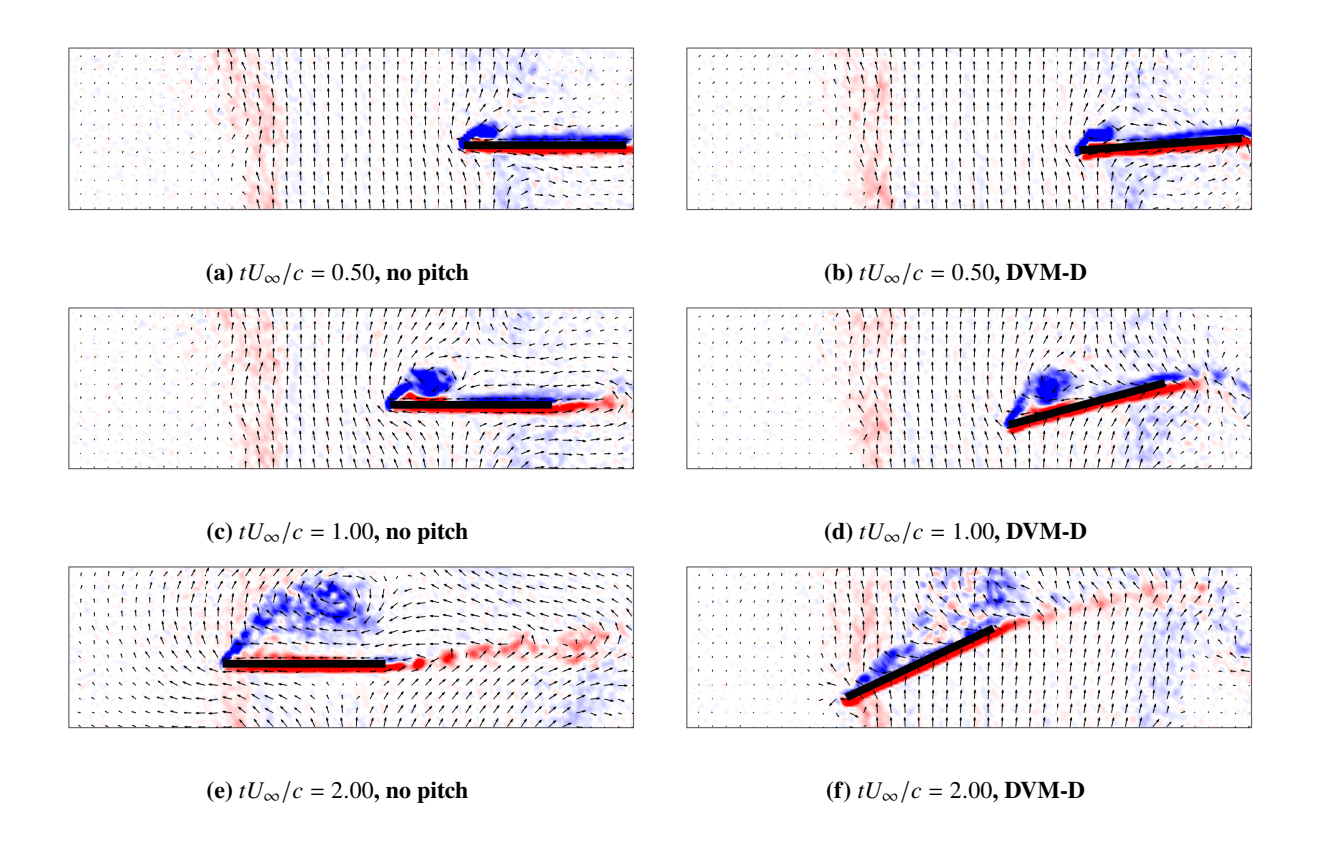


Fig. 7 The velocity and vorticity fields for GR = 0.25 without pitching and with DVM-D pitching



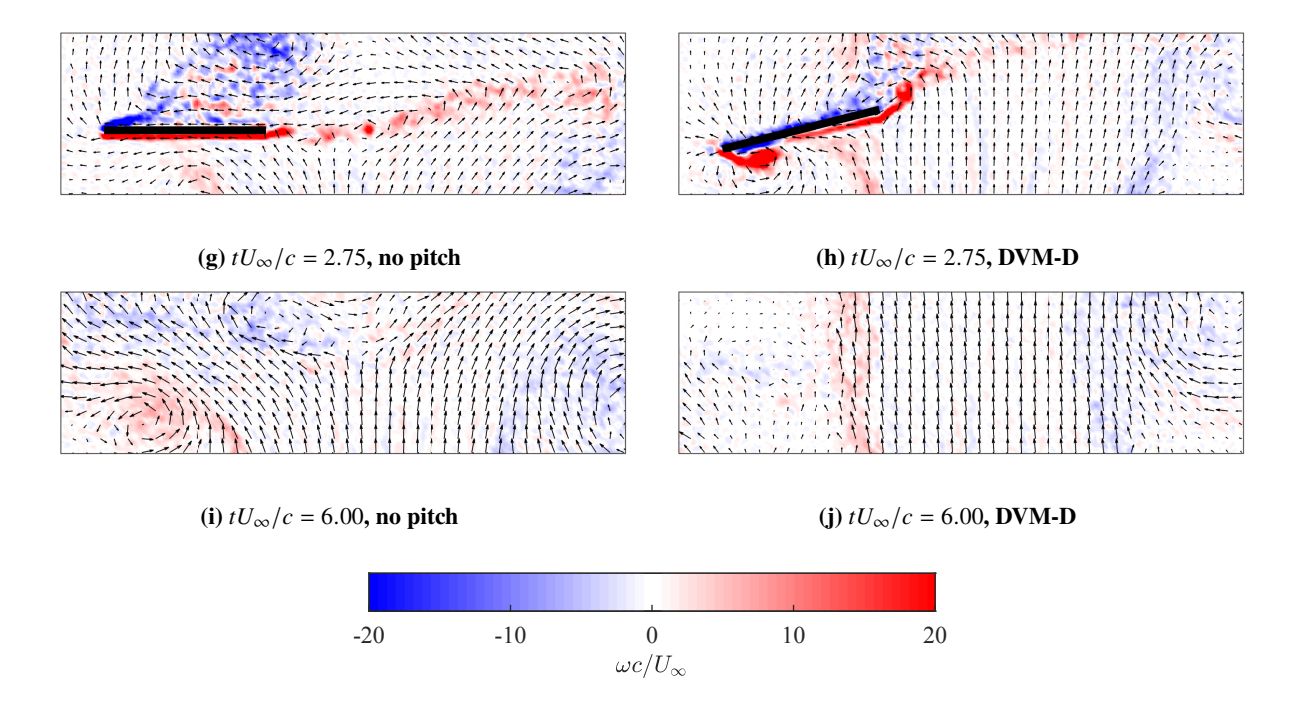


Fig. 8 The velocity and vorticity fields for GR = 0.50 without pitching and with DVM-D pitching

C. Circulatory forces and trends for the leading-edge vortex

The circulation of the suction-side and the pressure-side LEVs were calculated by defining the LEV region of interest in every PIV frame and integrating the vorticity within it. The LEV region of interest includes the vortex as well the shear layer that feeds it. Figure 9 shows the non-dimensional vortex circulation strength of the suction-side and pressure-side LEVs normalized by GR for all gust ratios and pitch maneuvers. Each maneuver is shown with a different color and each GR is shown with a different line marker. The circulation of the suction-side LEV circulation appears on the left half of the plot and the circulation of the pressure-side LEV circulation appears after $tU_{\infty}/c = 2$. The non-dimensional vortex circulation strength demonstrates a collapse when normalized by GR. The circulation strength of the suction-side LEV initially increases linearly for all cases. At $tU_{\infty}/c = 1.00$, the rate of increase of the suction-side LEV strength for all maneuvers except for the 'No pitch' maneuver decreases, and the circulations begin to plateau. This plateau corresponds with the instant the suction-side LEV separates from its feeding shear layers. The circulation of the suction-side LEVs in the non-maneuvering cases continues to linearly trend upwards until it begins to plateau at $tU_{\infty}/c = 1.75$. The plateau also corresponds to the detachment of the LEV from its shear layer. At $tU_{\infty}/c = 2$, a pressure-side LEV begins to form for the pitching maneuvers as the wing pitches up while exiting the gust. The magnitude increase of the vortex is initially linear and plateaus towards the end of the maneuver.

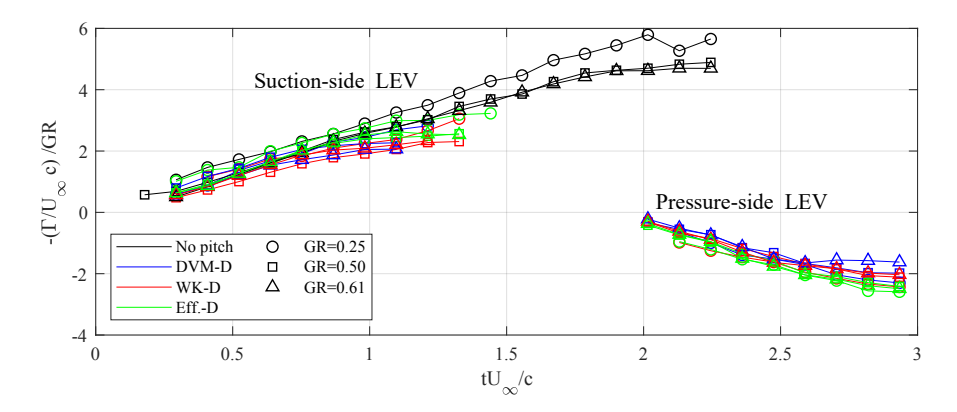


Fig. 9 Suction-side and pressure-side LEV strengths for the for all cases

for the DVM-D maneuvers, Fig. 10 shows the non-dimensional vortex circulation strength of the suction-side and pressure-side LEVs normalized by GR, as well as $C_L^{\rm rem}$ for all gust ratios tested. The maximum of $C_L^{\rm rem}$ corresponds with the presence of the suction-side LEV and the minimum $C_L^{\rm rem}$ corresponds with the presence of the pressure-side LEV. A lag of the LEV peak strengths after the $C_L^{\rm rem}$ magnitude peaks can be observed. The $C_L^{\rm rem}$ peak magnitudes always precede the LEV circulation peak magnitudes. This lag can be explained via the impulse formulation by Wu [19]. The lift can be expressed as a function of the time rate of change of the flow's impulse, which is a function of the vortex circulation strength as well as its time rate of change. Even though the circulation strength at the peak of $C_L^{\rm rem}$ is not at its maximum, its rate of change is. A delay of the circulation increase is also seen in Wagner's step response, in which the bound circulation begins at 0, but the lift response starts off at 50% of its final value [20].

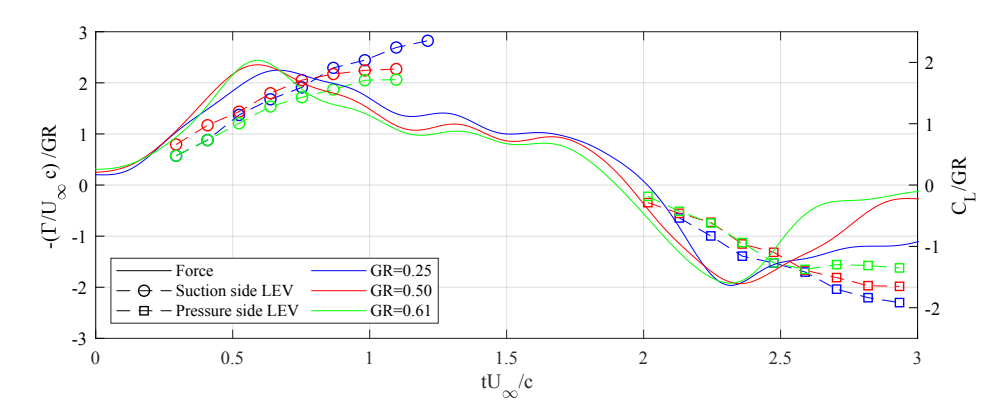


Fig. 10 Suction-side and pressure-side LEV strength and C_L^{rem} for the DVM-D maneuvers

D. Streamlines

The flowfield can be visualized using instantaneous streamlines, which can also highlight regions in the flow with large path curvature and flow stagnation. The streamlines presented in this section are computed from the PIV velocity vector fields using the algorithm presented by Jobard and Lefer [21]. Figure 11 presents the unsteady streamlines in the lab frame for the no-pitch and DVM-D cases at GR = 0.50 and $tU_{\infty}/c = 1.30$. In the no-pitch case in Fig. 11a, the vertical gust flow stagnates on the high pressure side of the wing and is diverted to flow horizontally. On the suction-side, the LEV is present and still attached at $tU_{\infty}/c = 1.30$. In Fig. 11b, the streamlines for the DVM-D maneuver do not experience stagnation on the high pressure side of the wing and thus remain relatively vertical compared to the no-pitch case. The vortex in the DVM-D case has detached and thus its core is further from the leading edge. For the non-maneuvering wing, the stagnation of flow on the high pressure side of the wing leads to high streamline curvature under the wing. Pressure increases across streamlines, outward from the center of curvature, to maintain the centripetal acceleration required for fluid parcels to follow the curved path. This positive gradient leads to high pressure on the

wing's pressure side. The streamlines in the pitching case exhibit less curvature, and thus the pressure does not increase as much as the 'no-pitch' case. The distinct streamline behavior between the two cases demonstrated in Fig. 11 suggests that the utilization of sensors on the high pressure side of the wing may provide useful information for flow sensing and control during mitigation of gust encounters.

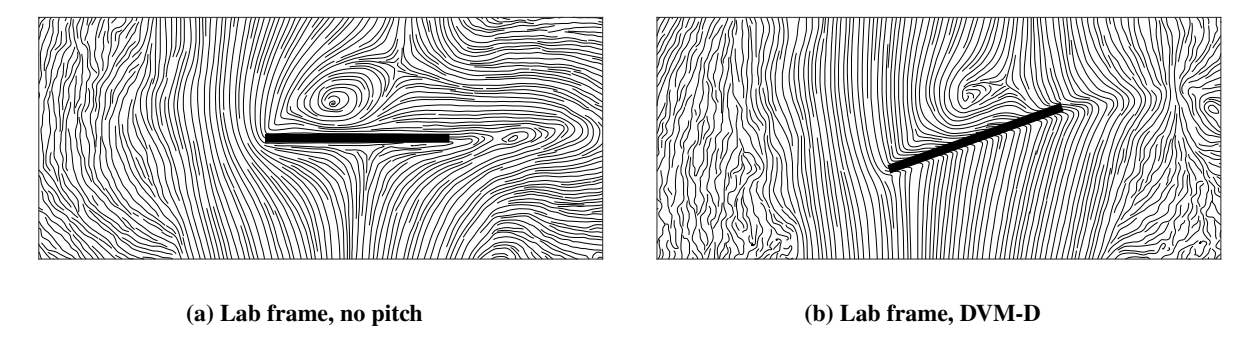


Fig. 11 Flow streamlines in the lab frame for GR = 0.50 and $tU_{\infty}/c = 1.30$

The streamlines in the lab frame present an intuitive method to understanding the topological difference in the flow from the perspective of the gust, but on-board flow sensing requires the frame of reference to be in the body frame of the wing. Figure 12 presents the the unsteady streamlines presented in Fig. 11 in the wing's frame of reference. The wing's body fame translates and rotates with the wing. The figure also presents colored contours of the flow speed in the body frame. The stagnation points in the flow are highlighted by the red contours in the figures. Without pitching, the gust introduces an effective angle of attack at the leading edge. Due to the angle of incidence of the flow, the stagnation point of the flow lies on the pressure side of the wing towards the leading edge. On the other hand, the pitching wing lines itself up with the flow, moving the stagnation point to the front of the leading edge. This observation presents a practical objective for gust mitigation through the control of stagnation point position on the wing. Since the stagnation point position on the wing is an indication of the local angle of attack at the leading edge of the wing, it may be possible to use surface pressure sensors and an on-board controller to maintain the position of the stagnation point throughout the gust encounter, thereby minimizing the excursion of the local angle of attack at the leading edge during the encounter.

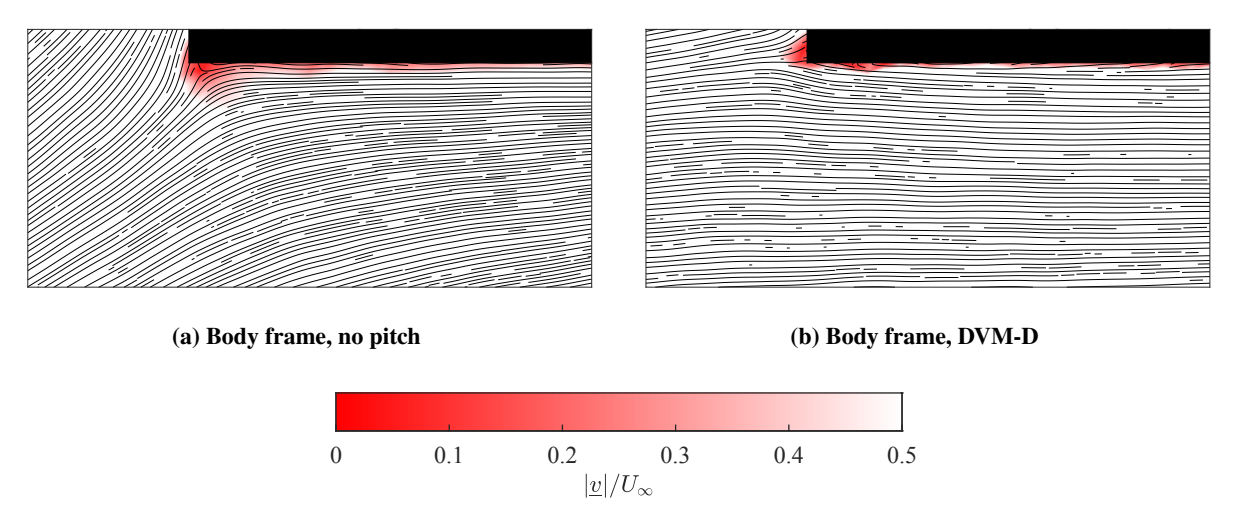


Fig. 12 Flow streamlines in the body frame of the wing for GR = 0.50 and $tU_{\infty}/c = 1.30$

E. Comparison of DVM-simulated and experimental flowfields

Figure 13 shows a comparison between the experimental flowfield and DVM simulation for a wing-gust encounter at GR = 0.50 undergoing a DVM-D maneuver. Although the discrete vortex method provides Lagrangian vortex positions, the DVM velocity field is evaluated on an Eulerian grid to match the PIV flowfields. The vorticity is then

calculated by taking the curl of the velocity field, $\omega = \nabla \times \vec{v}$. The flowfields show good qualitative agreement with slight differences in the time of vortex detachment. As the wing enters the gust, an LEV forms in the experiments and simulations. At $tU_{\infty}/c = 1.00$, the LEV begins to detach from the leading-edge in the experimental flowfield, however, it remains attached in the DVM simulations. Note that the DVM simulations fail to model the secondary vorticity that can be seen under the suction-side LEV in experiments. Since the DVM only sheds vorticity at the leading and trailing edges, it does not model vorticity that forms between the main vortex and the wing's surface. Medina and Jones [22] observed that the region of secondary vorticity under the LEV grows and eventually penetrates the leading-edge vortex, separating the LEV from the feeding shear layer. This aspect of the flow is not modeled in a DVM, and thus leads to a delayed detachment of the vortex. The detached vortex quickly loses its form in the experimental data, as shown in $tU_{\infty}/c = 2.00$, but it maintains its shape in the DVM solution. The detached vortex in the DVM maintains its coherence, perhaps due to the absence of three-dimensional effects in the simulation. At $tU_{\infty}/c = 2.75$, both flowfields exhibit the formation of a pressure-side LEV as well as a trailing-edge vortex.

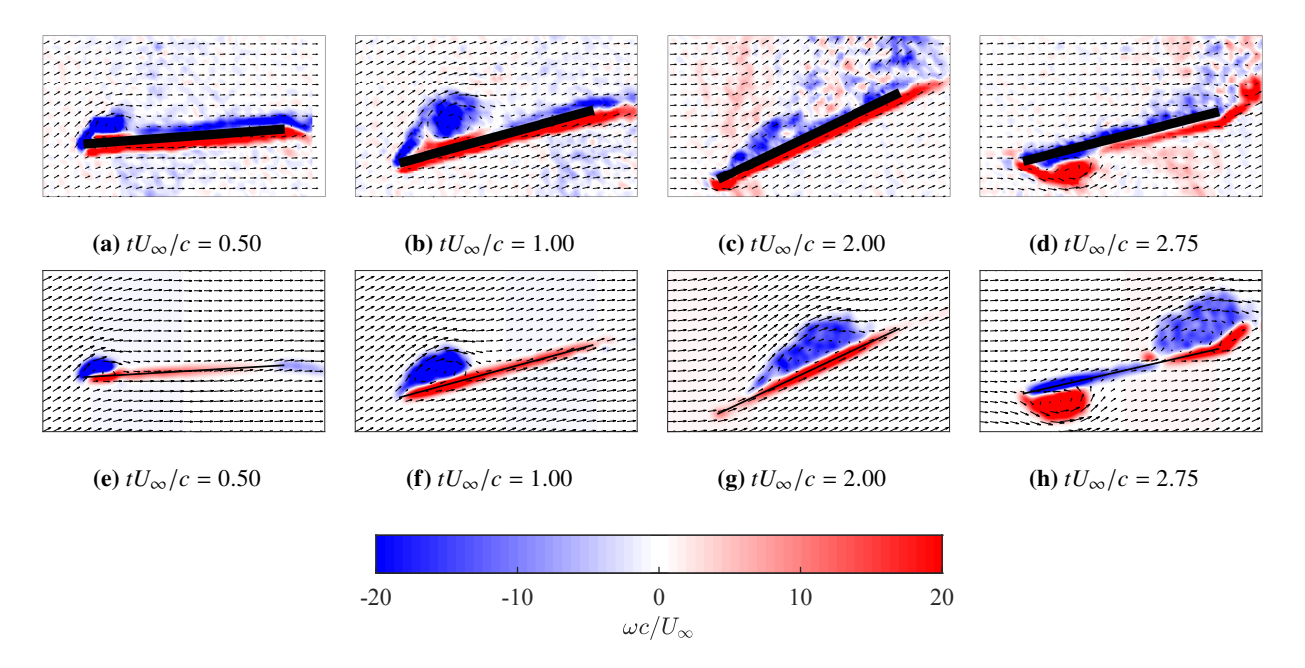


Fig. 13 A comparison between the experimental (top row) and DVM simulation (bottom row) flowfields of a wing-gust encounter at GR = 0.50 undergoing a DVM-D maneuver

The accuracy of the DVM simulation can be explored further by comparing the suction-side and pressure-side LEV strength between the experiments and DVM simulations. Figure 14 presents this comparison for the DVM-D maneuver for all gust ratios. The trends plotted between $tU_{\infty}/c = 0$ and $tU_{\infty}/c = 1.50$ are for the suction-side LEV and the trends plotted between $tU_{\infty}/c = 2.00$ and $tU_{\infty}/c = 3.00$ are for the pressure-side LEV. At the lowest gust ratio GR = 0.25, the DVM over-predicts the circulation contained in each vortex. In contrast, the DVM does a good job at predicting the circulation strength of the vortices at the higher gust ratios. The angle of incidence at the leading edge for the lowest gust ratio is small, and the flow does not fully separate. Thus, the application of the Kutta condition at the leading edge for this case leads to an over-prediction in the circulation shed, even though the wing has a sharp leading edge. On the other hand, the Kutta condition is successful at predicting the circulation shed from the leading edge at the higher gust ratios.

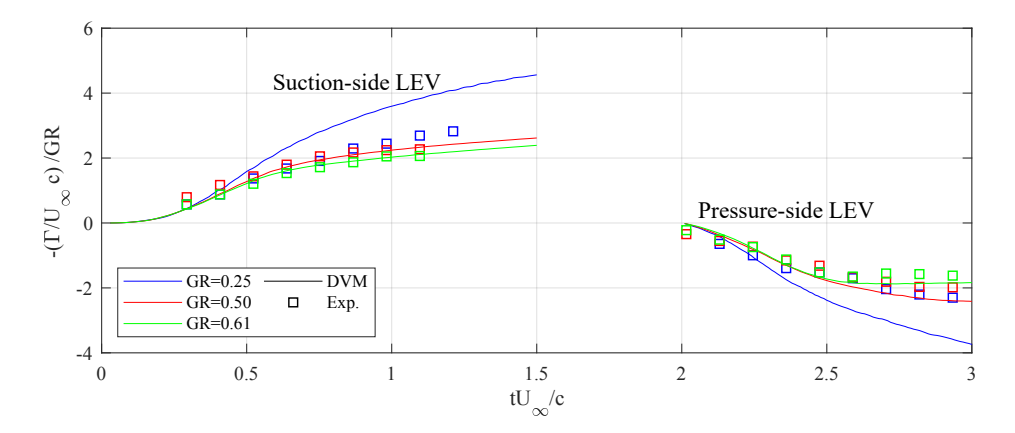


Fig. 14 Comparison of the suction-side and pressure-side LEV strengths for experiments and DVM simulations

V. Conclusion

This paper constructs and experimentally implements three open-loop mid-chord pitch maneuvers with the objective of mitigating the lift transient during large-amplitude transverse wing-gust encounters. The first maneuver 'Eff.-D' is designed such that the instantaneous geometric angle of attack opposes the effective angle of attack induced by the gust. The second maneuver 'WK-D' is designed such that the analytical lift result from an unsteady aerodynamic model based on the work of Wagner and Küssner sums to zero. The third maneuver 'DVM-D' is obtained from closed-loop control simulations in an unsteady discrete vortex model.

The total lift C_L is decomposed to an added-mass force contribution $C_L^{\rm am}$ and a contribution based on the remainder of the flow $C_L^{\rm rem}$. The remainder contribution contains the circulatory contribution due to the vortex shedding behavior of the wing as well as a non-circulatory contribution due to the flowfield imposed by the gust. Force results are shown to collapse when normalized by the gust ratio value. The cases undergoing the Eff.-D maneuvers perform the worst at mitigating the influence of the gust. The DVM-D and the WK-D maneuvers perform significantly better. The performance difference across maneuvers is shown to be dominated by the added-mass force. The pitching maneuvers partially attenuate the circulatory force experienced by the wing and counter-balance the remainder through the added-mass force contribution.

The flowfields of the no-pitch maneuvers and DVM-D are qualitatively compared at GR = 0.25 and GR = 0.50. As the wing enters the gust without pitching, it experiences a large upwash, creating a strong leading-edge shear layer which leads to the development of an suction-side LEV. The LEV grows until it sheds towards the latter part of the gust. The transverse gust flow stagnates on the pressure side of the wing, resulting in a large disturbance to the gust structure. This disturbance leads to a large transfer of momentum between the gust and the passing wing, increasing the lift transient experienced by the wing. As the wing with DVM-D pitching enters the gust, it starts to pitch down, and an LEV develops. The LEV detaches earlier and convects away for the maneuvering wing. As the wing exits the gust, it pitches up and a pressure-side LEV forms. In contrast with the case without pitching, the flow on the pressure side does not experience stagnation, thus minimizing the disturbance to the gust's flowfield.

The non-dimensional vortex circulation strength demonstrates a collapse when normalized by GR. The magnitude of the circulation strength of the suction-side and pressure-side LEV initially increases linearly for all cases, plateauing near vortex detachment. A lag is found for the circulation strengths of the suction- and pressure-side vortices after the peaks in C_L^{rem}

The unsteady streamlines are computed from the PIV vector fields and presented in the lab frame and the wing's body frame. In the lab frame, the vertical gust flow stagnates on the pressure side of the wing for the no-pitch case. For the DVM-D case, the flow does not experience stagnation on the pressure side of the wing. Without pitching, the flow encounters the wing at an angle in the wing's body frame. Thus streamlines presented in the body frame show a stagnation point of the flow lying on the pressure side of the wing. The wing undergoing the DVM-D maneuver aligns itself with the flow leading to the stagnation point moving towards the front of the leading edge.

The accuracy of discrete vortex models (DVMs) for maneuver design is examined by comparing the DVM simulated flow fields with experimental PIV measurements. It is found that the flowfields show good qualitative agreement. The

main discrepancies found are due to the DVM not modeling the secondary vorticity observed under the LEV and 3D flow effects seen in experiments. The accuracy of the DVM simulation can be explored further by comparing the suction-side and pressure-side LEV strengths between the experiments and DVM simulations. At the lowest gust ratio GR = 0.25, the DVM over-predicts the circulation strengths of these vortices. However, the DVM does a good job at predicting the circulation strength of the vortices at higher gust ratios (e.g. GR = 0.5, 0.61).

Acknowledgments

The authors thank Ignacio Andreu and Oliver Wilde for valuable discussions. The authors also gratefully acknowledge support from the Air Force Office of Scientific Research under grant FA9550-16-1-0508 and the National Science Foundation under award numbers 2003951 and 2003999.

References

- [1] Moulin, B., and Karpel, M., "Gust loads alleviation using special control surfaces," *Journal of Aircraft*, Vol. 44, No. 1, 2007, pp. 17–25.
- [2] Pines, D. J., and Bohorquez, F., "Challenges facing future micro-air-vehicle development," *Journal of Aircraft*, Vol. 43, No. 2, 2006, pp. 290–305.
- [3] Zarovy, S., Costello, M., Mehta, A., Gremillion, G., Miller, D., Ranganathan, B., Humbert, J. S., and Samuel, P., "Experimental study of gust effects on micro air vehicles," *AIAA Atmospheric Flight Mechanics Conference, Toronto, ON*, August, 2010, p. 7818.
- [4] Jones, A. R., "Gust encounters of rigid wings: Taming the parameter space," *Physical Review Fluids*, Vol. 5, No. 11, 2020, p. 110513.
- [5] Küssner, H. G., "Stresses produced in airplane wings by gusts," Tech. Rep. 645, NACA, 1932.
- [6] Wagner, H., "Über die Entstehung des dynamischen Auftriebes von Tragflügeln," ZAMM Journal of Applied Mathematics and Mechanics / Zeitschrift für Angewandte Mathematik und Mechanik, Vol. 5, No. 1, 1925, pp. 17–35.
- [7] Biler, H., Badrya, C., and Jones, A. R., "Experimental and computational investigation of transverse gust encounters," *AIAA Journal*, Vol. 57, No. 11, 2019, pp. 4608–4622.
- [8] Ellington, C. P., Van Den Berg, C., Willmott, A. P., and Thomas, A. L., "Leading-edge vortices in insect flight," *Nature*, Vol. 384, No. 6610, 1996, pp. 626–630.
- [9] Perrotta, G., and Jones, A. R., "Unsteady forcing on a flat-plate wing in large transverse gusts," *Experiments in Fluids*, Vol. 58, No. 8, 2017, pp. 1–11.
- [10] Corkery, S. J., Babinsky, H., and Harvey, J. K., "On the development and early observations from a towing tank-based transverse wing—gust encounter test rig," *Experiments in Fluids*, Vol. 59, No. 9, 2018, p. 135.
- [11] Andreu-Angulo, I., Babinsky, H., Biler, H., Sedky, G., and Jones, A. R., "Effect of transverse gust velocity profiles," *AIAA Journal*, Vol. 58, No. 12, 2020, pp. 5123–5133.
- [12] Sedky, G., Lagor, F. D., and Jones, A., "Unsteady aerodynamics of lift regulation during a transverse gust encounter," *Physical Review Fluids*, Vol. 5, No. 7, 2020, p. 074701.
- [13] Andreu Angulo, I., and Babinsky, H., "Unsteady modelling of pitching wings for gust mitigation," *AIAA Scitech 2021 Forum*, 2021.
- [14] Sedky, G., Jones, A. R., and Lagor, F. D., "Lift regulation during transverse gust encounters using a modified Goman–Khrabrov model," AIAA Journal, Vol. 58, No. 9, 2020, pp. 3788–3798.
- [15] Leishman, G. J., Principles of helicopter aerodynamics, Cambridge University Press, 2006.
- [16] Jones, R. T., "The unsteady lift of a wing of finite aspect ratio," Tech. Rep. 681, NACA, 1940.
- [17] Sears, W. R., and Sparks, B. O., "On the reaction of an elastic wing to vertical gusts," *Journal of the Aeronautical Sciences*, Vol. 9, No. 2, 1941, pp. 64–81.

- [18] Sedky, G., Biler, H., and Jones, A. R., "Experimental comparison of a sinusoidal and trapezoidal transverse gust," *AIAA Journal*, Under review.
- [19] Wu, J. C., "Theory for aerodynamic force and moment in viscous flows," AIAA Journal, Vol. 19, No. 4, 1981, pp. 432–441.
- [20] Taha, H. E., and Rezaei, A. S., "On the high-frequency response of unsteady lift and circulation: A dynamical systems perspective," *Journal of Fluids and Structures*, Vol. 93, 2020, p. 102868.
- [21] Jobard, B., and Lefer, W., "Creating evenly-spaced streamlines of arbitrary density," *Visualization in Scientific Computing* '97, Springer, 1997, pp. 43–55.
- [22] Medina, A., and Jones, A. R., "Leading-edge vortex burst on a low-aspect-ratio rotating flat plate," *Physical Review Fluids*, Vol. 1, No. 4, 2016, p. 044501.